

Comparison of geomagnetic aided navigation algorithms for hypersonic vehicles^{*}

Kai CHEN[†], Wen-chao LIANG, Ming-xin LIU, Han-yan SUN

School of Astronautics, Northwestern Polytechnical University, Xi'an 710072, China

[†]E-mail: chenkai@nwpu.edu.cn

Received Dec. 27, 2019; Revision accepted Mar. 16, 2020; Crosschecked July 21, 2020; Published online Aug. 13, 2020

Abstract: In this paper, we simulate, verify, and compare the performance of three classical geomagnetic matching aided navigation algorithms to assess their applicability to hypersonic vehicle navigation. Firstly, we introduce the various sources of the geomagnetic field. Secondly, we describe the principles and processes of the geomagnetic contour matching (MAGCOM) algorithm, iterative closest contour point (ICCP) algorithm, and Sandia inertial magnetic aided navigation (SIMAN) algorithm. Thirdly, we discuss the principles of inertial/geomagnetic integrated navigation, and propose the state and observation equations of integrated navigation. Finally, we perform a simulation of inertial/geomagnetic integrated navigation on the hypersonic boost-glide vehicle trajectory. The simulation results indicate that the real-time performance of the SIMAN algorithm can be optimized such that the matching accuracy is higher than that of the other two algorithms. At the same time, the SIMAN algorithm can achieve better stability, and though the amount of measurement noise can be larger, it can still achieve good positioning accuracy.

Key words: Geomagnetic navigation; Contour; Geomagnetic elements; Integrated navigation; Kalman filter

<https://doi.org/10.1631/jzus.A1900648>


CLC number: V44

1 Introduction

Near space refers to the airspace within an altitude of 20–100 km. Compared with traditional aeronautical space, near space can provide more abundant information, faster communication, and more accurate resolution (Chen, 2017; Wang et al., 2018; Wen et al., 2019). In virtue of their high velocity, large scope of activities, fast responses, cross space operation capability, and good invisibility and elusiveness, near space hypersonic vehicles can present extraordinary advantages in military applications and have become a hot topic of study (Li et al., 2017; Lv et al., 2017; Liao et al., 2018; Wang YY et al., 2019).

Currently, the navigation of hypersonic vehicles relies on the strapdown inertial navigation system (SINS) and global navigation satellite system (GNSS), which are limited by poor concealment because the reception of electromagnetic signals by the satellite positioning system requires a receiver (Montenbruck et al., 2018). The satellite positioning system may also lead to signal loss, as well as carrier phase lock loss of hypersonic vehicles. The simultaneous loss of necessary information from multiple satellites may be observed during vehicle operations. The application of inertial/celestial integrated navigation (SINS/CNS) to hypersonic vehicles is still in its infancy. Moreover, problems with aero-optical effects and stray light induced by complicated flow fields near the vehicle are yet to be resolved (Lu and Yang, 2018; Zhang et al., 2018). Inertial/terrain integrated navigation (SINS/TAN) is not applicable in areas with minor topographical fluctuations (Ma et al., 2018).

^{*} Project supported by the Space Science and Technology Innovation Fund of China (No. 2016KC020028) and the Fund of China Space Science and Technology (No. 2017-HT-XG)

 ORCID: Kai CHEN, <https://orcid.org/0000-0002-2586-7546>

© Zhejiang University and Springer-Verlag GmbH Germany, part of Springer Nature 2020

Geomagnetic navigation, which has become a hot topic, is an autonomous navigation technique with advantages such as all day, all weather, and all terrain operations without accumulated errors. Indeed, the utility of using the geomagnetic field for navigation is seen across the animal kingdom, for instance, allowing many types of marine animals to undertake long-distance migrations (Putman, 2018). Owing to the rapid development of geomagnetic navigation technology, the number of categories of geomagnetic navigation algorithms and improved algorithms has increased drastically. For instance, Xiao et al. (2018a) proposed a geomagnetic matching iterative closest contour point (ICCP) algorithm based on probability data association, where effective matching results are combined based on the statistical characteristics of the measurement errors of the geomagnetic field, to improve the positioning accuracy of the ICCP algorithm. Wang CY et al. (2019) proposed a geomagnetic matching algorithm involving simulated annealing based constrained particle swarm optimization to enhance the accuracy and efficiency of geomagnetic matching. Zhou et al. (2019) proposed a geomagnetic gradient bionic navigation system based on a parallel approximation method, which can achieve effective navigation without a non-priori geomagnetic reference map, by estimating the heading angel of the carrier.

Owing to the high flight altitude, high speed, and large space span of near space hypersonic vehicles, the navigation and positioning accuracies of different geomagnetic navigation algorithms can vary significantly different. To validate the applicability of such algorithms to the navigation of hypersonic vehicles, the hypersonic boost-glide vehicle trajectory was simulated by three mature geomagnetic aided navigation algorithms (geomagnetic contour matching (MAGCOM), ICCP, and Sandia inertial magnetic aided navigation (SIMAN) algorithms). Their applicability to the navigation of hypersonic vehicles was also investigated.

2 Geomagnetic matching algorithms

2.1 Background on geomagnetic field

Geomagnetism is a natural magnetic phenomenon observed on earth, and the magnetic field of the

earth is called the earth magnetic field, also known as geomagnetic field (Chen et al., 2018). The geomagnetic field is a relatively stabilized magnetic field developed by the superposition of magnetic fields from different sources. Using \mathbf{r} to represent the position vector and t to represent the time, the earth magnetic field $\mathbf{B}(\mathbf{r}, t)$ can be divided into three parts: the main earth magnetic field $\mathbf{B}_m(\mathbf{r}, t)$, the geomagnetic abnormal field $\mathbf{B}_c(\mathbf{r}, t)$ (also known as the crustal magnetic field), and the disturbance field $\mathbf{B}_d(\mathbf{r}, t)$:

$$\mathbf{B}(\mathbf{r}, t) = \mathbf{B}_m(\mathbf{r}, t) + \mathbf{B}_c(\mathbf{r}, t) + \mathbf{B}_d(\mathbf{r}, t). \quad (1)$$

The main earth magnetic field and the geomagnetic abnormal field, both of which are stable, could be used for geomagnetic matching navigation. The cruising altitude range of near space hypersonic vehicles is about 20–30 km, where the geomagnetic abnormal field has negligible intensity, while the disturbance field can be a source of interference in navigation. Therefore, the geomagnetic navigation of hypersonic vehicles relies on the main earth magnetic field (Zong et al., 2018).

2.2 MAGCOM algorithm

The MAGCOM algorithm (Zhang, 2016) essentially searches for the optimized matching point in the designated objective function in the matching area based on a specific relevant metric (Xiao et al., 2018b). In this study, the mean square difference (MSD) correlation degree with good noise resistance and moderate calculation (He et al., 2016) was selected as the metric of the MAGCOM algorithm. The measuring sequence was labeled as

$$M_{\text{mea}} = \{m_{\text{mea}}^l \mid l = 1, 2, \dots, L\}, \quad (2)$$

and the reference sequence extracted from point (i, j) in the matching area was labeled as

$$M_{\text{map}} = \{m_{\text{map}}^l(i, j) \mid l = 1, 2, \dots, L; (i, j) \in P \times Q\}, \quad (3)$$

where L represents the length of the matching sequence, l represents the sequence number of matching point, and $P \times Q$ represents the size of the matching area.

$R(\beta)$ can be defined as a direction cosine matrix with rotation angle β :

$$R(\beta) = \begin{bmatrix} \cos \beta & \sin \beta \\ -\sin \beta & \cos \beta \end{bmatrix}. \quad (4)$$

The coordinate sequence of the original trajectory can be defined as $\{(i_l, j_l) | l=1, 2, \dots, L\}$ while the center point of rotation can be defined as $[i_0, j_0]$. The coordinate sequence of trajectory after rotation can be defined as $\{(i'_l, j'_l) | l=1, 2, \dots, L\}$, such that

$$[i'_l, j'_l]^T = R(\beta)[i_l - i_0, j_l - j_0]^T + [i_0, j_0]^T. \quad (5)$$

The geomagnetic reference value of the trajectory after rotation is defined as $M'_{\text{map}} = \{m'_{\text{map}}(i'_l, j'_l) | l=1, 2, \dots, L\}$.

To match the M'_{map} , the MSD can be calculated as follows:

$$\text{MSD}_{ij}^\beta = \frac{1}{L} \sum_{l=1}^L [m'_{\text{map}}(i'_l, j'_l) - m_{\text{mea}}^l]^2, \quad \beta \in [-\theta, \theta], \quad (6)$$

where θ represents the maximum rotation angle.

Fig. 1 illustrates the principles of the MAGCOM algorithm which consists of four steps:

(1) Define the output of the SINS as the reference sequence $X_n = \{x_n | n=1, 2, \dots, L\}$, where x_n is each SINS output point, and the geomagnetic value of the corresponding point measured by the magnetometer as $M_{\text{mea}} = \{m_{\text{mea}}^l | l=1, 2, \dots, L\}$.

(2) The possible area of carrier motion can be obtained according to the accuracy and the working period of SINS, and is defined as the matching area. The geomagnetic reference sequence of this position $M_{\text{map}} = \{m_{\text{map}}^l(i, j) | l=1, 2, \dots, L\}$ can be obtained from the geomagnetic map in the carrier.

(3) The SINS trajectory X_n is translated within the matching range. After each translation, geomagnetic reference data and M_{mea} of the trajectory can be processed by MSD calculation and the sequence is rotated with the step of $\beta \in [-\theta, \theta]$. After each rotation, geomagnetic reference data and M_{mea} of the trajectory are processed by MSD calculation to obtain MSD_{ij}^β .

(4) Execute the traverse of the reference sequences within the entire matching area to select the trajectory sequence with the minimum MSD_{ij}^β as the final matching result.

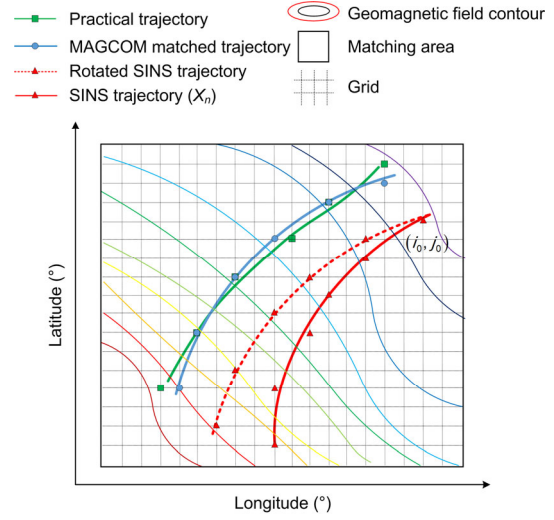


Fig. 1 Schematic of the MAGCOM algorithm

2.3 ICCP algorithm

Originating from image matching algorithms, the ICCP algorithm is essentially the transformation of the output trajectory by SINS to the nearest points between the measuring sequence contour cluster and the reference trajectory (Wu et al., 2018). Song et al. (2016) clarified the principles of the ICCP algorithm.

The output vehicle trajectory can be defined by SINS as $X_n = \{x_n | n=1, 2, \dots, L\}$, and the practical vehicle trajectory can be defined as $Y_n = \{y_n | n=1, 2, \dots, L\}$, where y_n is each practical point. The real-time magnetic sequence measured by a magnetometer is defined as $M_{\text{mea}} = \{m_{\text{mea}}^l | l=1, 2, \dots, L\}$.

Fig. 2 illustrates the principles of the ICCP algorithm, which consists of the following four steps:

(1) The value-equivalent contour clusters of corresponding geomagnetic values can be searched in the geomagnetic reference map according to the M_{mea} measured by the magnetometer.

(2) The points in the contour cluster nearest to the SINS trajectory X_n are labeled as the matching sequence $A_n = \{a_n | n=1, 2, \dots, L\}$, where a_n represents each matching point.

(3) The rigid transformation matrix (T) corresponding to the minimum distance from TX_n to A_n can be searched. In addition, $X_n=TX_n$, a new A_n in the contour cluster and T can be searched. Using $d(p, q)$ to represent the distance between points p and q , if $J(A_n, TX_n) = \sum_{n=1}^L d^2(a_n, Tx_n)$ is below a critical value (ε) or the maximum iteration number is reached, the iteration should be terminated.

(4) The ultimate TX_n is regarded as the corrected trajectory.

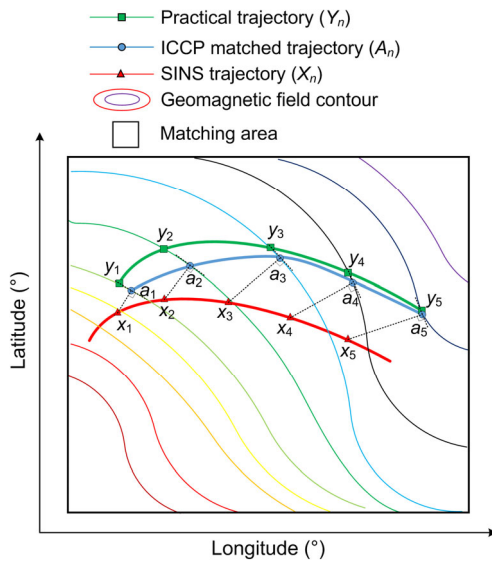


Fig. 2 Schematic of the ICCP algorithm

2.4 SIMAN algorithm

In the SIMAN algorithm, the trajectory is continuously corrected by the application of a recursive Kalman filter according to the difference between geomagnetic values measured by the magnetometer and the inertial navigation system. Wei et al. (2017) clarified the principles of both the SIMAN algorithm and nine-point plane fitting.

2.4.1 Establishment of the state equation

In the SIMAN system, the state vector is selected according to the state parameters to be estimated (Wang et al., 2017). In this study, the latitude error (δL) and longitude error ($\delta \lambda$) of geomagnetic aided navigation were selected as the state vector for the development of the corresponding state equation:

$$\delta X_{k+1} = \Phi \delta X_k + W_k, \quad (7)$$

where the state vector (δX_k) refers to the state to be estimated and $\delta X_k = [\delta L, \delta \lambda]^T$; k represents the discrete time. $\Phi = [1, 0; 0, 1]$ refers to the state transfer matrix. W_k is the driving noise.

2.4.2 Establishment of the observation equation

In the SIMAN algorithm, the geomagnetic intensity, which is the function value of the position, is regarded as the observation value. If the position provided by SINS is $(\hat{L}, \hat{\lambda})$, the geomagnetic reference value of this position $m_{\text{map}}(\hat{L}, \hat{\lambda})$ can be obtained according to the geomagnetic reference map. Meanwhile, geomagnetic measurement value $m_{\text{mea}}(L, \lambda)$ at the practical position (L, λ) can be obtained by the magnetometer. Since the geomagnetic reference map is a mathematic model developed based on measurement data, $m_{\text{map}}(\hat{L}, \hat{\lambda})$ and $m_{\text{mea}}(\hat{L}, \hat{\lambda})$ satisfy:

$$m_{\text{map}}(\hat{L}, \hat{\lambda}) = m_{\text{mea}}(\hat{L}, \hat{\lambda}) + V_m, \quad (8)$$

where V_m is the geomagnetic reference map measurement and model quantization noise.

The observation equation can be revised as

$$\begin{aligned} Z &= m_{\text{map}}(\hat{L}, \hat{\lambda}) - m_{\text{mea}}(L, \lambda) \\ &= m_{\text{mea}}(\hat{L}, \hat{\lambda}) + V_m - m_{\text{mea}}(L, \lambda). \end{aligned} \quad (9)$$

If the position error is selected as the state vector ($\delta X_k = [\delta L, \delta \lambda]^T$), then

$$\begin{aligned} m_{\text{mea}}(\hat{L}, \hat{\lambda}) &= m_{\text{mea}}(L + \delta L, \lambda + \delta \lambda) \\ &= m_{\text{mea}}(L, \lambda) + \frac{\partial m_{\text{mea}}(L, \lambda)}{\partial L} \delta L \\ &\quad + \frac{\partial m_{\text{mea}}(L, \lambda)}{\partial \lambda} \delta \lambda + V_1, \end{aligned} \quad (10)$$

where V_1 refers to the linear error.

By substituting Eq. (10) into Eq. (9), the observation equation can be expressed as

$$Z = \frac{\partial m_{\text{mea}}(L, \lambda)}{\partial L} \delta L + \frac{\partial m_{\text{mea}}(L, \lambda)}{\partial \lambda} \delta \lambda + V_1 + V_m. \quad (11)$$

$h_L = \partial m_{\text{mea}}(L, \lambda) / \partial L$ and $h_\lambda = \partial m_{\text{mea}}(L, \lambda) / \partial \lambda$ refer to the latitude and the longitude slopes, respectively. $V = V_m + V_l$ refers to the observation noise. The observation equation can be expressed as

$$Z = H\delta X_k + V, \quad (12)$$

where $H = [h_L, h_\lambda]$ can be obtained by nine-point plane fitting.

Fig. 3 illustrates the principles of the SIMAN algorithm, which consists of four steps:

(1) The matching area is designated according to the indications by SINS and the corresponding geomagnetic reference, where the value $m_{\text{map}}(\hat{L}, \hat{\lambda})$ is identified. The difference between $m_{\text{map}}(\hat{L}, \hat{\lambda})$ and $m_{\text{mea}}(L, \lambda)$ is defined as Z .

(2) The geomagnetic reference map in the matching area is linearized by nine-point plane fitting according to the indications by SINS to obtain h_L and h_λ .

(3) Z is regarded as the measurement input of the Kalman filter, and $[h_L, h_\lambda]$ is regarded as the observation matrix of the Kalman filter. The filtering calculation can be performed by the Kalman filter, given the initial state vector δX_0 and covariance matrix P_0 .

(4) SINS is compensated and corrected according to the output of filter (δX_k).

3 Inertial/geomagnetic integrated navigation algorithm

3.1 Principles of integrated navigation

First, the trajectory of the near space vehicle is planned. Then, an appropriate geomagnetic component is selected according to the geomagnetic information of the trajectory area for the development of a numerical geomagnetic reference map, which is stored in the navigation computer system of the vehicle. The matching feature value can be obtained in real time by the application of the three-axial magnetometer on the vehicle. Furthermore, a matching area with appropriate size can be selected according to the reference trajectory generated by SINS for geomagnetic matching. The geomagnetic matching result can be regarded as the outputs of the geomagnetic navigation system or filtered with the result of SINS to obtain the outputs of the inertial/geomagnetic integrated navigation system. The procedures of the integrated navigation algorithm are summarized in Fig. 4.

3.2 Kalman filter

3.2.1 Establishment of the state equation

The state equation of the Kalman filter is:

$$\dot{X}(t) = F(t)X(t) + G(t)W(t), \quad (13)$$

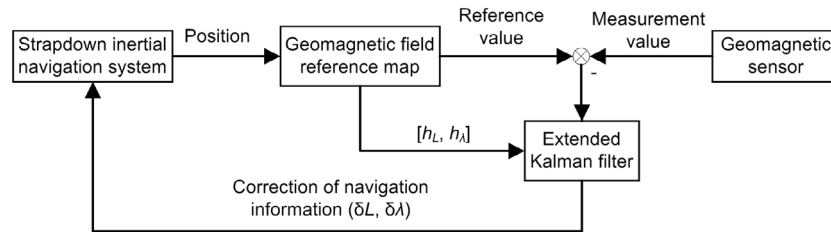


Fig. 3 Schematic of the SIMAN algorithm

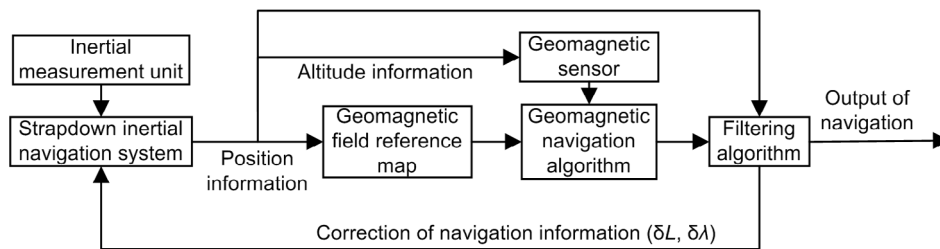


Fig. 4 Block diagram of the inertial/geomagnetic integrated navigation system

where $X(t)$ is the error state variable of the system developed with the geographical coordinate system as the navigation coordinate system at moment t :

$$\begin{aligned} X &= [\phi, \delta V, \delta P, \varepsilon, \nabla]^T, \\ \phi &= [\phi_E, \phi_N, \phi_U]^T, \\ \delta V &= [\delta v_E, \delta v_N, \delta v_U]^T, \\ \delta P &= [\delta \lambda, \delta L, \delta h]^T, \\ \varepsilon &= [\varepsilon_{bx}, \varepsilon_{by}, \varepsilon_{bz}]^T, \\ \nabla &= [\nabla_{bx}, \nabla_{by}, \nabla_{bz}]^T, \end{aligned} \quad (14)$$

where ϕ_E, ϕ_N , and ϕ_U are the east, north, and upward attitude error angles, respectively; $\delta v_E, \delta v_N$, and δv_U are the east, north, and upward velocity errors, respectively; $\delta \lambda, \delta L$, and δh are the longitude, latitude, and altitude errors, respectively; $\varepsilon_{bx}, \varepsilon_{by}$, and ε_{bz} are three-axial gyro constant drift errors; ∇_{bx}, ∇_{by} , and ∇_{bz} are three-axial accelerometer bias errors.

$F(t)$ is the system state transfer matrix:

$$F(t) = \begin{bmatrix} F_N & F_S \\ \mathbf{0}_{6 \times 9} & F_M \end{bmatrix}, \quad (15)$$

where F_N is the corresponding 9D basic navigation parameter system matrix. F_S and F_M can be expressed as

$$F_S = \begin{bmatrix} C_b^n & \mathbf{0}_{3 \times 3} \\ \mathbf{0}_{3 \times 3} & C_b^n \\ \mathbf{0}_{3 \times 3} & \mathbf{0}_{3 \times 3} \end{bmatrix}, \quad F_M = [\mathbf{0}_{6 \times 6}], \quad (16)$$

where C_b^n represents the attitude matrix.

$G(t)$ is the noise transfer matrix:

$$G(t) = \begin{bmatrix} C_b^n & \mathbf{0}_{3 \times 3} \\ \mathbf{0}_{3 \times 3} & C_b^n \\ \mathbf{0}_{9 \times 3} & \mathbf{0}_{9 \times 3} \end{bmatrix}_{15 \times 6}. \quad (17)$$

$W(t)$ is the white noise error matrix, which consists of random errors of the gyroscope and accelerometer:

$$W(t) = [w_{\varepsilon_x}, w_{\varepsilon_y}, w_{\varepsilon_z}, w_{\nabla_x}, w_{\nabla_y}, w_{\nabla_z}]^T, \quad (18)$$

where $w_{\varepsilon_x}, w_{\varepsilon_y}$, and w_{ε_z} are random errors of three axes of gyroscope, respectively; $w_{\nabla_x}, w_{\nabla_y}$, and w_{∇_z} are random errors of three axes of accelerometer, respectively.

3.2.2 Establishment of the observation equation

The observation equation can be expressed as

$$Z(t) = H(t)X(t) + V(t). \quad (19)$$

The output position of geomagnetic matching is horizontal without information about the altitude, so the altitude errors of SINS cannot be effectively corrected. Hence, a barometric altimeter is introduced into the altitude channel to correct the errors of output altitude information from SINS.

Therefore, Z predicted by the Kalman filtering observation equation consists of the difference between the horizontal position generated by SINS and the geomagnetic matching (Z_1), as well as the difference between the altitude information generated by SINS and the altimeter (Z_2). Z_1 and Z_2 are defined as follows:

$$\begin{aligned} Z_1 &= \begin{bmatrix} L_s - L_m \\ \lambda_s - \lambda_m \end{bmatrix}, \\ Z_2 &= [h_s - h_m], \end{aligned} \quad (20)$$

where λ_s, L_s , and h_s are longitude, latitude, and altitude information generated by SINS, respectively, λ_m and L_m are the longitude and latitude information, respectively, generated by geomagnetic matching, and h_m is the altitude of the near space hypersonic vehicle generated by the barometric altimeter. Hence,

$$Z = \begin{bmatrix} Z_1 \\ Z_2 \end{bmatrix} = \begin{bmatrix} L_s - L_m \\ \lambda_s - \lambda_m \\ h_s - h_m \end{bmatrix}. \quad (21)$$

$H(t)$ is the observation matrix:

$$H(t) = [H_{11} \ H_{12} \ H_{13} \ H_{14} \ H_{15}]^T, \quad (22)$$

where

$$H_{11} = H_{12} = H_{14} = H_{15} = \mathbf{0}_{3 \times 3}, \quad (23)$$

$$\mathbf{H}_{13} = \begin{bmatrix} 1 & 0 & 0 \\ 0 & 1 & 0 \\ 0 & 0 & 1 \end{bmatrix}. \quad (24)$$

$\mathbf{V}(t)$ is the observation noise matrix of geomagnetic matching:

$$\mathbf{Z} = \begin{bmatrix} L_s - L_m \\ \lambda_s - \lambda_m \\ h_s - h_m \end{bmatrix} = \begin{bmatrix} \delta L - \delta L_m \\ \delta \lambda - \delta \lambda_m \\ \delta h - \delta h_m \end{bmatrix} = \begin{bmatrix} \delta L \\ \delta \lambda \\ \delta h \end{bmatrix} - \begin{bmatrix} \delta L_m \\ \delta \lambda_m \\ \delta h_m \end{bmatrix}. \quad (25)$$

Hence,

$$\mathbf{V}(t) = \begin{bmatrix} \delta L_m \\ \delta \lambda_m \\ \delta h_m \end{bmatrix}, \quad (26)$$

where $\delta \lambda_m$, δL_m , and δh_m are respectively longitude and latitude errors generated by geomagnetic matching, and altitude errors generated by the barometric altimeter.

4 Simulations

In this study, the geomagnetic map generated by the World Magnetic Model (NCEI, 2019) was applied (Qi et al., 2017). The altitude was 25 km, the latitude range was 40° N–48° N, and the longitude range was 109° E–112° E. The grid resolution was 0.01 (°)/grid. After the interpolation of the geomagnetic map, the grid resolution of the ultimate geomagnetic map was 0.00125 (°)/grid.

The flight of hypersonic boost-glide vehicles in near space can be divided into different phases: the boost phase, free ballistic phase, ballistic re-entry phase, ballistic pull-up phase, and equilibrium gliding phase (Chen et al., 2019). Herein, the ballistic trajectory can be simplified, as this study focused on the geomagnetic navigation of hypersonic vehicles at the equilibrium gliding phase. We assumed that the vehicle could accelerate, climb, and glide at constant speed, and turn left and turn right successively. The gliding speed was 2000 m/s, and the simulation duration was 790 s. The ballistic trajectory is presented in Fig. 5.

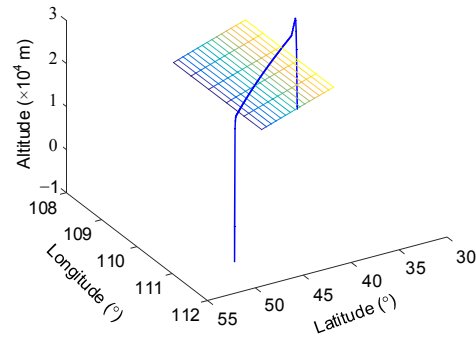


Fig. 5 Trajectory and geomagnetic navigation area of near space hypersonic vehicles

In the navigation simulation of the near space hypersonic vehicles during the equilibrium gliding phase, the 0–420 s stage is pure inertial navigation, and the 420–790 s stage is inertial/geomagnetic integrated navigation. The sampling interval of magnetometers was 1 s; the sampling interval of accelerometers and gyroscopes was 10 ms; the period of Kalman filtering in integrated navigation was 1 s.

Table 1 shows the parameters for the SINS (Chen et al., 2020).

Table 1 Parameters for the strapdown inertial navigation system (SINS)

Simulation parameter	Value
Gyroscope constant drift error ((°)/h)	0.05
Gyroscope random error ((°)/h ^{1/2})	0.05
Gyroscope scale factor error	5×10 ⁻⁵
Accelerometer constant bias	1×10 ⁻⁴ g ₀
Accelerometer random error	1×10 ⁻⁵ g ₀
Accelerometer scale factor error	1×10 ⁻⁴
Initial roll angle, yaw, and pitch errors (°)	60, 20, 20
Initial velocity error (m/s)	0.05
Initial position error (m)	5

Note: g_0 represents standard acceleration of gravity. Reprinted from (Chen et al., 2020), Copyright 2020, with permission from Elsevier

The magnetometer may be quite accurate after calibration (this process is also significant), but due to the time-varying characteristic of the geomagnetic field and the interpolation/model error of the geomagnetic reference map, it is unlikely that the geomagnetic measurement value will coincide exactly with the value of the geomagnetic reference map at

the same position. The focus of this study was the applicability of the three algorithms in hypersonic vehicle navigation. Therefore, four mag error levels were set for the simulation: ± 0.1 nT, ± 1 nT, ± 5 nT, and ± 10 nT. They represent the range of the difference between the true value of the geomagnetism and the geomagnetic reference map.

Table 2 lists other simulation parameters for geomagnetic matching.

Table 2 Parameters for geomagnetic matching

Parameter	Value
MAGCOM	
Matching sequence length	10
Matching area size (grid)	25×25
Rotation angle range (°)	[-10, 10]
Rotation step (°)	1
ICCP	
Matching sequence length	5
Matching area size (grid)	300×300
Maximum iteration number	20
Critical distance (m)	200
SIMAN	
δX_0	[0, 0; 0, 0]
P_0	[1, 0; 0, 1]

As shown in Figs. 6–9, the error of the pure inertial navigation system increased with the time range at the 0–420 s stage. At the 420–790 s stage, the geomagnetic navigation system was initiated and the error of the integrated navigation system decreased drastically. At the mag error level of ± 1 nT, the MAGCOM algorithm was exposed to the divergence and did not work properly, while the positioning accuracies of the SIMAN algorithm and the ICCP algorithm remained constant (the SIMAN algorithm exhibited the minimum error). At the mag error level of ± 5 nT, the ICCP algorithm was exposed to the divergence, while the SIMAN algorithm still worked properly: its absolute mean latitude and longitude errors were only about 249 m and 397 m, respectively. Table 3 indicates the duration required by the three algorithms and their errors. As observed, the SIMAN algorithm was optimized and real-time in nature, while the ICCP algorithm needed a long duration as it requires contour generation. The duration needed by the MAGCOM algorithm was determined by the size of matching area and the length of

matching sequence. In order of decreasing sensor accuracy, stability, and reliability, the three algorithms followed the sequence: SIMAN>ICCP>MAGCOM.

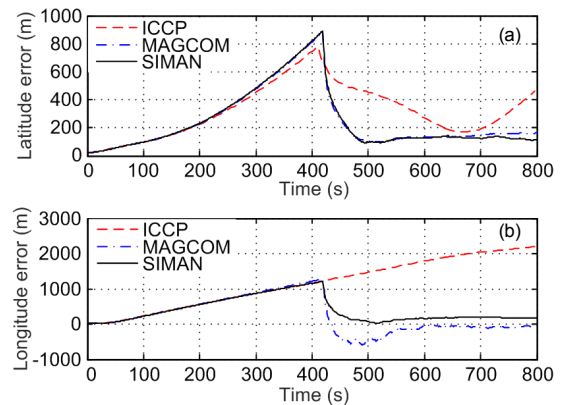


Fig. 6 Analysis of integrated navigation errors at mag error level of ± 0.1 nT: (a) latitude error; (b) longitude error

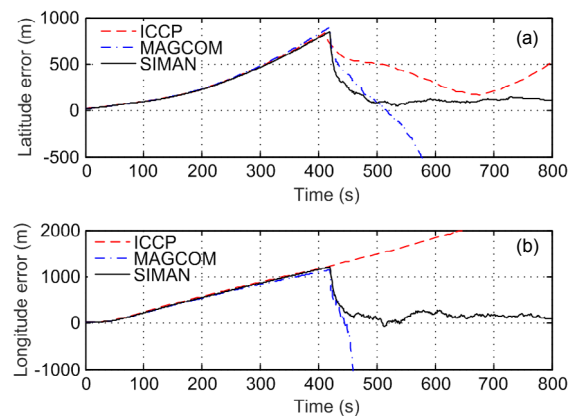


Fig. 7 Analysis of integrated navigation errors at mag error level of ± 1 nT: (a) latitude error; (b) longitude error

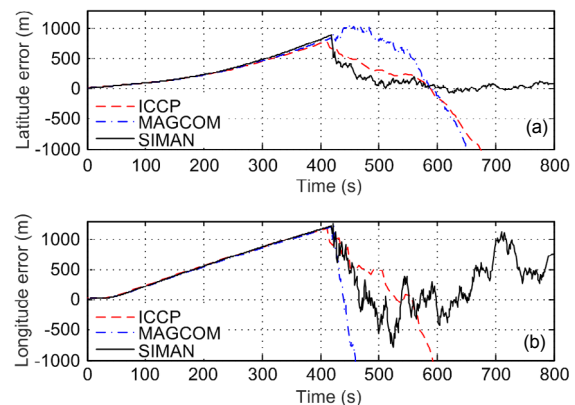


Fig. 8 Analysis of integrated navigation errors at mag error level of ± 5 nT: (a) latitude error; (b) longitude error

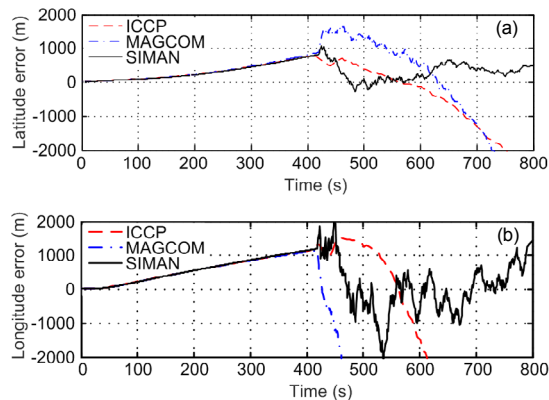


Fig. 9 Analysis of integrated navigation errors at mag error level of ± 10 nT: (a) latitude error; (b) longitude error

Table 3 Absolute mean errors of inertial/geomagnetic integrated navigation during the 420–790 s stage

Integrated navigation	Dura- tion (s)	Mag error level (nT)	Absolute mean latitude error (m)	Absolute mean longitude error (m)
SINS/ MAGCOM	13.8722	± 0.1	162.6191	194.8881
		± 1	1456.1120	Divergence
		± 5	1505.4120	Divergence
		± 10	Divergence	Divergence
SINS/ ICCP	15.9434	± 0.1	343.4247	1732.646
		± 1	372.1157	1798.634
		± 5	727.4169	3536.847
		± 10	749.1818	3979.623
SINS/ SIMAN	6.5993	± 0.1	154.6980	182.5864
		± 1	155.0434	184.2774
		± 5	249.4415	396.5313
		± 10	321.6272	575.6865

5 Conclusions

In this paper, we have presented a summary of the procedures of three classical geomagnetic navigation algorithms for the navigation of near space hypersonic vehicles, and simulations of integrated navigations. The simulation results of the different integrated navigation systems were analyzed and their applications to the navigation of hypersonic vehicles compared. According to the simulation results, the SIMAN algorithm was superior to the other two algorithms in terms of its real-time nature, positioning accuracy, reliability, and stability.

Some parts of the geomagnetic field change rapidly and irregularly, and there is interference from

the hypersonic vehicles to the magnetometer. Thus, for better results, there is still some work that needs to be done, including the following:

1. Simulations are performed under different geomagnetic models, which may contain more information about geomagnetic anomalies or short-term changes in the geomagnetic field, to verify the sensitivity and stability of these algorithms.

2. When the geomagnetic model is very accurate, the calibration of the magnetometer may become the main factor affecting the accuracy of navigation. The magnetometer model in the simulation should be improved, including analysis of the interference with the hypersonic vehicles (materials with different metals, shapes, and structures), establishment of a magnetic interference model, and verification of the corresponding compensation method.

Contributors

Kai CHEN designed the research. Wen-chao LIANG processed the corresponding data and wrote the first draft of the manuscript. Ming-xin LIU helped to organize the manuscript. Han-yan SUN revised and edited the final version.

Conflict of interest

Kai CHEN, Wen-chao LIANG, Ming-xin LIU, and Han-yan SUN declare that they have no conflict of interest.

References

- Chen K, 2017. Strapdown inertial navigation algorithm for hypersonic boost-glide vehicle. 21st AIAA International Space Planes and Hypersonics Technologies Conference, Article 2174.
<https://doi.org/10.2514/6.2017-2174>
- Chen K, Shen FQ, Sun HY, et al., 2019. Hypersonic vehicle navigation algorithm in launch centered earth-fixed frame. *Journal of Astronautics*, 40(10):1212-1218 (in Chinese).
- Chen K, Zhou J, Shen FQ, et al., 2020. Hypersonic boost-glide vehicle strapdown inertial navigation system/global positioning system algorithm in a launch-centered earth-fixed frame. *Aerospace Science and Technology*, 98: 105679.
<https://doi.org/10.1016/j.ast.2020.105679>
- Chen Z, Zhang Q, Pan MC, et al., 2018. A new geomagnetic matching navigation method based on multidimensional vector elements of earth's magnetic field. *IEEE Geoscience and Remote Sensing Letters*, 15(8):1289-1293.
<https://doi.org/10.1109/LGRS.2018.2836465>
- He YP, Liu XX, Cai YP, et al., 2016. Research on aided navigation based on terrain elevation matching and simulation.

- Proceedings of the Photoelectronic Technology Committee Conferences, Article 97962X.
<https://doi.org/10.1117/12.2230690>
- Li L, Wang GH, Yu HB, et al., 2017. A TBD algorithm for near space hypersonic target. *Journal of Astronautics*, 38(4):420-427 (in Chinese).
<https://doi.org/10.3873/j.issn.1000-1328.2017.04.012>
- Liao L, Yan L, Huang W, et al., 2018. Mode transition process in a typical strut-based scramjet combustor based on a parametric study. *Journal of Zhejiang University-SCIENCE A (Applied Physics & Engineering)*, 19(6): 431-451.
<https://doi.org/10.1631/jzus.A1700617>
- Lu JZ, Yang L, 2018. Optimal scheme of star observation of missile-borne inertial navigation system/stellar refraction integrated navigation. *Review of Scientific Instruments*, 89(5):054501.
<https://doi.org/10.1063/1.5020226>
- Lv Z, Xia ZX, Liu B, et al., 2017. Preliminary experimental study on solid-fuel rocket scramjet combustor. *Journal of Zhejiang University-SCIENCE A (Applied Physics & Engineering)*, 18(2):106-112.
<https://doi.org/10.1631/jzus.A1600489>
- Ma T, Li Y, Jiang YQ, et al., 2018. A dynamic path planning method for terrain-aided navigation of autonomous underwater vehicles. *Measurement Science and Technology*, 29(9):095105.
<https://doi.org/10.1088/1361-6501/aad466>
- Montenbruck O, Steigenberger P, Hauschild A, 2018. Multi-GNSS signal-in-space range error assessment—methodology and results. *Advances in Space Research*, 61(12):3020-3038.
<https://doi.org/10.1016/j.asr.2018.03.041>
- NCEI (National Centers for Environmental Information), 2019. The World Magnetic Model. NCEI, USA.
<https://www.ngdc.noaa.gov/geomag/WMM/index.html>
- Putman N, 2018. Marine migrations. *Current Biology*, 28(17): R972-R976.
<https://doi.org/10.1016/j.cub.2018.07.036>
- Qi XK, Ye DX, Sun YZ, et al., 2017. Simulations to true animals' long-distance geomagnetic navigation. *IEEE Transactions on Magnetics*, 53(1):5200108.
<https://doi.org/10.1109/TMAG.2016.2600540>
- Song ZG, Zhang JS, Zhu WQ, et al., 2016. The vector matching method in geomagnetic aiding navigation. *Sensors*, 16(7):1120.
<https://doi.org/10.3390/s16071120>
- Wang CY, Wang CY, Ji CJ, 2019. A simulated annealing based constrained particle swarm optimization algorithm for geomagnetic matching. *Electronic Design Engineering*, 27(7):153-157 (in Chinese).
<https://doi.org/10.3969/j.issn.1674-6236.2019.07.033>
- Wang JX, Li YZ, Yu XK, et al., 2018. Investigation of heat transfer mechanism of low environmental pressure large-space spray cooling for near-space flight systems. *International Journal of Heat and Mass Transfer*, 119: 496-507.
<https://doi.org/10.1016/j.ijheatmasstransfer.2017.11.128>
- Wang SP, Zhao JH, Wu ZY, 2017. A Study of Key Positioning Technologies in Underwater Geomagnetic Matching Navigation. China University of Geosciences Press, Wuhan, China, p.149 (in Chinese).
- Wang YY, Yang XX, Yan HC, 2019. Reliable fuzzy tracking control of near-space hypersonic vehicle using aperiodic measurement information. *IEEE Transactions on Industrial Electronics*, 66(12):9439-9447.
<https://doi.org/10.1109/TIE.2019.2892696>
- Wei EH, Dong CJ, Yang YL, et al., 2017. A robust solution of integrated SITAN with TERCOM algorithm: weight-reducing iteration technique for underwater vehicles' gravity-aided inertial navigation system. *Navigation*, 64(1):111-122.
<https://doi.org/10.1002/navi.176>
- Wen X, Liu J, Li J, et al., 2019. Design and numerical simulation of a clamshell-shaped inlet cover for air-breathing hypersonic vehicles. *Journal of Zhejiang University-SCIENCE A (Applied Physics & Engineering)*, 20(5): 347-357.
<https://doi.org/10.1631/jzus.A1800620>
- Wu FH, Zhang Q, Pan MC, et al., 2018. Study on geomagnetic vector matching algorithm based on ICCP. *China Measurement & Test*, 44(2):103-107 (in Chinese).
<https://doi.org/10.11857/j.issn.1674-5124.2018.02.021>
- Xiao J, Duan XS, Qi XH, 2018a. Iterated closest contour point algorithm for geomagnetic matching based on probability data association. *Journal of Chinese Inertial Technology*, 26(2):202-208 (in Chinese).
<https://doi.org/10.13695/j.cnki.12-1222/o3.2018.02.010>
- Xiao J, Qi XH, Duan XS, 2018b. Research of status of magnetic matching algorithms and its improvement strategies. *Electronics Optics & Control*, 25(1):55-59 (in Chinese).
- Zhang CX, Chen XF, Lu JZ, et al., 2018. Deep data fusion method for missile-borne inertial/celestial system. *AIP Conference Proceedings*, 1967(1):020014.
<https://doi.org/10.1063/1.5038986>
- Zhang XM, 2016. Theory and Application of Geomagnetic Navigation. National Defense Industry Press, Beijing, China, p.142-149 (in Chinese).
- Zhou J, Wang Q, Cheng C, 2019. Geomagnetic gradient bionic navigation based on the parallel approaching method. *Proceedings of the Institution of Mechanical Engineers, Part G: Journal of Aerospace Engineering*, 233(9):3131-3140.
<https://doi.org/10.1177/0954410018793290>
- Zong H, Liu Y, Yang Y, 2018. Overview of the research status about geomagnetic navigation technology. *Aerospace Control*, 36(3):93-98 (in Chinese).
<https://doi.org/10.16804/j.cnki.issn1006-3242.2018.03.015>

中文概要

题目：高超声速飞行器的地磁匹配辅助导航算法比较

目的：验证三种经典的地磁匹配辅助导航算法在临近空间高超声速飞行器导航中的适用性。探讨和比较地磁轮廓匹配 (MAGCOM)、沿等值线最近点迭代 (ICCP) 和桑迪亚地磁辅助导航 (SIMAN) 算法在助推-滑翔高超声速飞行器导航中的实时性、稳定性和定位精度。

创新点：比较分析助推-滑翔高超声速飞行器上的三种地磁匹配算法，并讨论其适用性。

方法：1. 分析地球磁场组成部分的时变特性，并选取地球主磁场作为地磁匹配辅助导航的地磁基准图。

2. 根据三种地磁匹配算法的原理，分别总结出三种算法的流程和步骤；根据惯性/地磁组合导航的原理，给出组合导航的状态方程和观测方程。

3. 根据世界地磁场模型 (WMM) 得出地磁基准图，并在简化的助推-滑翔飞行器弹道上对三种算法在不同的磁误差条件下进行仿真验证和比较。

结论：1. 在磁误差很小的情况下，SIMAN 算法和 MAGCOM 算法的定位精度都很高；在磁误差较大的情况下，SIMAN 算法的精度最高。

2. SIMAN 算法的稳定性最好，而 MAGCOM 算法的稳定性最差。3. SIMAN 算法的实时性最好，而 ICCP 算法的实时性最差。

关键词：地磁导航；等值线；地磁要素；组合导航；卡尔曼滤波